Magnetic order induces symmetry breaking in the single-crystalline orthorhombic CuMnAs semimetal

Eve Emmanouilidou,[1] Huibo Cao,[2] Peizhe Tang,[3] Xin Gui,[4] Chaowei Hu,[1] Bing Shen,[1] Junyi Wu,[1] Shou-Cheng Zhang,[3,5] Weiwei Xie,[4] and Ni Ni[1,*]

[1]*Department of Physics and Astronomy and California NanoSystems Institute, University of California, Los Angeles, California 90095, USA*
[2]*Quantum Condensed Matter Division, Oak Ridge National Laboratory, Oak Ridge, Tennessee 37831, USA*
[3]*Department of Physics, McCullough Building, Stanford University, Stanford, California 94305-4045, USA*
[4]*Department of Chemistry, Louisiana State University, Baton Rouge, Louisiana 70803, USA*
[5]*Stanford Institute for Materials and Energy Sciences, SLAC National Accelerator Laboratory, Menlo Park, California 94025, USA*

(Received 23 August 2017; published 4 December 2017)

Recently, orthorhombic CuMnAs has been proposed to be a magnetic material where topological fermions exist around the Fermi level. Here we report the magnetic structure of the orthorhombic $Cu_{0.95}MnAs$ and $Cu_{0.98}Mn_{0.96}As$ single crystals. While $Cu_{0.95}MnAs$ is a commensurate antiferromagnet below 360 K with a propagation vector of $\mathbf{k} = 0$, $Cu_{0.98}Mn_{0.96}As$ undergoes a second-order paramagnetic to incommensurate antiferromagnetic phase transition at 320 K with $\mathbf{k} = (0.1,0,0)$, followed by a second-order incommensurate to commensurate antiferromagnetic phase transition at 230 K. In the commensurate antiferromagnetic state, the Mn spins order parallel to the crystallographic b axis but antiparallel to their nearest neighbors, with the spin orientation along the b axis. This magnetic order breaks S_{2z}, the two-fold rotational symmetry around the c axis, resulting in finite band gaps at the crossing point and the disappearance of the massless topological fermions. However, our first-principles calculations suggest that orthorhombic CuMnAs can still host spin-polarized surface states and signature induced by nontrivial topology, which makes it a promising candidate for antiferromagnetic spintronics.

DOI: 10.1103/PhysRevB.96.224405

I. INTRODUCTION

Recently, a lot of research interest has focused on the physics of Dirac fermions in the bulk material systems. The existence of these excitations in condensed-matter systems, which resemble massless fermions from high-energy physics, has been theoretically proposed and experimentally realized in numerous nonmagnetic materials, including Cd_3As_2 [1,2], Na_3Bi [3,4], etc. By breaking the inversion symmetry ($\mathcal{P}$) or the time-reversal symmetry ($\mathcal{T}$), a Dirac point can be split into a pair of Weyl points. To break $\mathcal{T}$, we can either apply an external magnetic field or use the spontaneous magnetic moment inside the material. In the latter case, the correlation between spontaneous magnetism and Weyl fermions has been studied in the AMnPn$_2$ (A = rare earth or alkali earth and Pn = Sb or Bi) system [5–12], the half-Heusler compound GdPtBi [13,14], and suggested in CeSbTe [15].

Magnetic CuMnAs compounds are proposed to host nontrivial topology [16,17]. CuMnAs has two polymorphs; the tetragonal (TET) CuMnAs, which crystalizes in the space group $P4/nmm$, and the orthorhombic (ORT) CuMnAs crystalizing in the $Pnma$ space group. The TET phase consists of alternating layers of edge-sharing $CuAs_4$ and $MnAs_4$ tetrahedra. It has been proposed to be a candidate with favorable applications in spintronics [18,19] and a topological metal-insulator transition driven by the Néel vector [17]. On the other hand, the ORT phase consists of a 3D network of edge-sharing $CuAs_4$ and $MnAs_4$ tetrahedra [Fig. 1(a)], where the Mn atoms form a 3D distorted honeycomb lattice [Fig. 1(b)]. ORT CuMnAs is proposed to be an antiferromagnetic topological massless Dirac semimetal even when the spin-orbit coupling (SOC) is fully considered [16]. The first-principles calculation shows that based on the theoretically proposed magnetic structure, although both the $\mathcal{T}$ and $\mathcal{P}$ symmetries are broken, their combination $\mathcal{PT}$ and the nonsymmorphic screw symmetry S_{2z}, which is the two-fold rotational symmetry around the c axis, are preserved. Based on the above symmetry assumptions, a gapless Dirac point is robust in the reciprocal space. Thus, the antiferromagnetic (AFM) ORT CuMnAs provides an ideal system to study the interplay between AFM and Dirac fermions [16].

In this paper, we focus on the ORT CuMnAs single crystals. The synthesis, resistivity, and susceptibility of polycrystalline ORT CuMnAs have been previously reported elsewhere [20]. However, the magnetic structure of ORT CuMnAs, which is crucial in the symmetry analysis to investigate the topology of the material, has not yet been experimentally determined. This is partially due to the challenge in synthesizing high quality samples. Indeed, several off-stoichiometric compounds, such as ORT $CuMn_3As_2$ and $Cu_2Mn_4As_3$ have been discovered [21], suggesting that the site mixing of Cu and Mn is difficult to control. Here we report the synthesis and characterization of single crystals of Cu_xMn_yAs. We experimentally determine its magnetic structure through neutron-diffraction experiments, and find that it indeed breaks the $\mathcal{T}$ and $\mathcal{P}$ symmetries but keeps their combination $\mathcal{PT}$. However, since the experimentally determined magnetic order breaks the S_{2z} symmetry, massless Dirac fermions are no longer robust. Our first-principles calculations further show that this magnetic order will cause ORT CuMnAs to host an interesting topological phase with spin-polarized surface states, which could be promising for spintronics applications.

*Corresponding author: nini@physics.ucla.edu

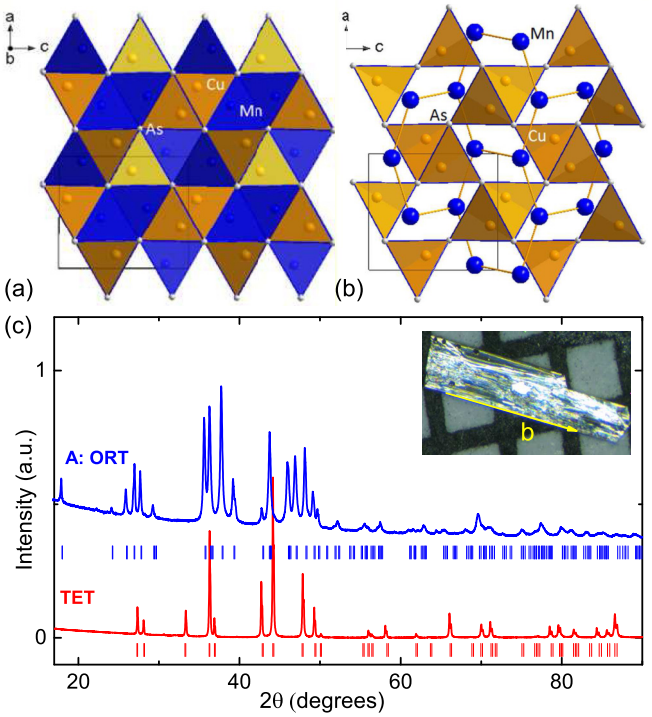

FIG. 1. (a), (b) Crystal structure of ORT CuMnAs. (a) $CuAs_4$ (orange) and $MnAs_4$ (blue) tetrahedral building blocks. (b)Distorted Mn honeycomb lattice is indicated (Mn in blue). (c) Powder x-ray-diffraction patterns of ORT (pulverized single crystals from batch A) and TET (from powder synthesis) phases. Ticks indicate the Bragg peak positions. Inset: A picture of an ORT single crystal against a mm sized grid. This as-grown surface is the *bc* plane.

II. MATERIAL SYNTHESIS AND EXPERIMENTAL METHODS

For the solid-state reaction, Cu, Mn, and As powders were mixed thoroughly and pressed into a pellet. The pellet was slowly heated to 600 °C and kept at that temperature overnight. It was then heated to 1000 °C, where it dwelled for 20 h, and finally quenched in water. Through powder x-ray-diffraction measurements [Fig. 1(c)] we found that stoichiometric or slightly less As leads to ORT CuMnAs phase, while 6% of extra As results in the TET phase and a slight amount of MnAs.

CuMnAs single crystals were grown via the high-temperature solution method with Bi as the flux [21,22]. Cu shots, Mn granules, As and Bi chunks were mixed together and placed inside a 5-ml alumina crucible. The alumina crucible was then placed inside an evacuated quartz tube with 1/3 Atm of Ar gas. The ampoule was subsequently heated to 1100 °C, held for 3 h, cooled to 850 °C in 2 h and then cooled to 400 °C at a rate of 3 °C/h. We additionally allowed the crystals to anneal at 400 °C for 0 or 24 h before the single crystals were separated from the flux using a centrifuge.

Table I summarizes the starting growth concentrations we have tried and the resultant phases of the single crystals. The CuMnAs single crystals have a rectangular platelike growth habit. The inset of Fig. 1(c) shows the picture of an ORT CuMnAs single crystal against a mm scale. Typical thickness of these single crystals is around 0.07 mm. The as-grown surface is the *bc* plane while the long axis of the plate is its *b* axis.

TABLE I. The growth conditions and crystal structure of Cu_xMn_yAs single crystals. For more details of dR/dT, please refer to Figs. 2(a) and 2(b) and the Supplemental Material [31]. $*$ means although only one resistive anomaly was observed, the temperature where it occurred is much lower than 360 K, the one for the polycrystalline sample.

Batch	Cu: Mn: As: Bi	Annealing time (h)	Structure	Kinks in dR/dT
A	1 : 1 : 0.9 : 12	0	ORT	1
B	1 : 1 : 1 : 12	24	ORT	2
C	1 : 1 : 1.1 :12	0	ORT	1* or 2
D	0.9 : 1 : 1 : 12	0	ORT	1* or 2
E	1.1 : 1 : 1 : 12	0	ORT	1*

Single-crystal x-ray-diffraction data were collected on a Bruker Apex II X-ray diffractometer with Mo radiation k_α ($\lambda = 0.710\,73$ Å). Intensities were extracted and corrected for Lorentz and polarization effects with the SAINT program. Numerical absorption corrections were accomplished with XPREP which is based on face-indexed absorption [23]. The twin unit cell was tested. With the SHELXTL package, the crystal structures were solved using direct methods and refined by full-matrix least-squares on F_2 [24].

Single-crystal neutron-diffraction measurements were carried out on the HB-3A four-circle diffractometer at the High Flux Isotope Reactor (HFIR), Oak Ridge National Laboratory (ORNL). The neutron wavelength was 1.546 Å from a bent Si-220 monochromator [25]. The magnetic symmetry analysis was carried out on the Bilbao Crystallographic Server [26] and the data were refined with FULLPROF Suite [27].

Electrical resistivity, Hall coefficient and heat capacity data were collected using a Quantum Design Physical Property Measurement System (QD PPMS Dynacool). The standard four-probe configuration was used. The susceptibility was measured with a QD Magnetic Properties Measurement System (QD MPMS). Around five single crystals with similar phase transitions were selected for both heat capacity and susceptibility measurements.

The first-principles calculations were carried out by density functional theory method with the projector augmented wave method [28], as implemented in the Vienna ab initio simulation package (VASP) [29]. The Perdew-Burke-Ernzerhof exchange-correlation functional and the plane-wave basis with energy cutoff of 300 eV were employed. The inner atomic positions of the lattice were allowed to be fully relaxed until the residual forces are less than 1×10^{-3} eV/Å. The Monkhorst-Pack k points were $9\times15\times9$, and SOC was included in self-consistent electronic structure calculations. The maximally localized Wannier functions were constructed to obtain the tight-binding Hamiltonian [30], which is used to calculate the bulk Fermi surface, surface electronic spectrum, and surface states.

III. EXPERIMENTAL RESULTS

The resistivities of the ORT single crystals we measured are around tenths of mΩ cm and show metallic behavior.

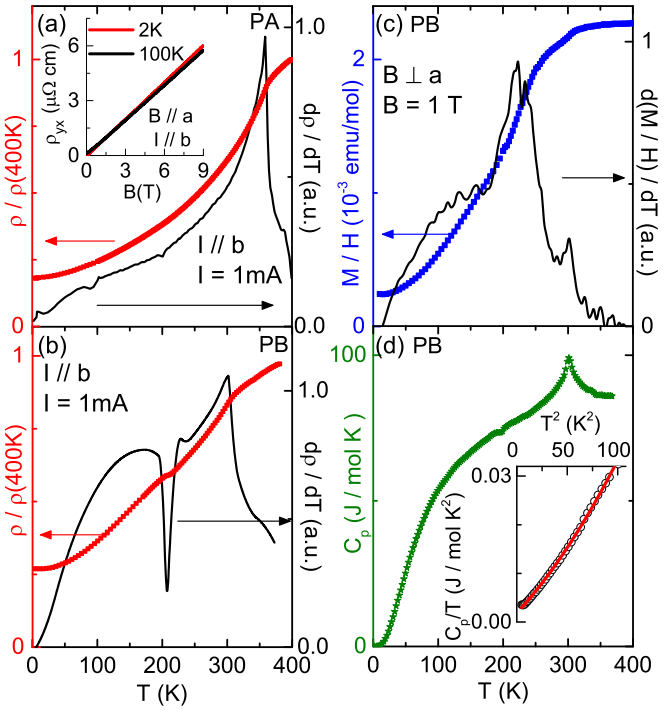

FIG. 2. PA: (a) Normalized resistivity ρ/ρ (400 K) and its derivative $d\rho/dT$ vs T. Inset: Hall resistivity ρ_{yx} vs T. PB [(b)–(d)] (b) Normalized resistivity ρ/ρ (400 K) and $d\rho/dT$ vs T. (c) Susceptibility M/H and $d(M/H)/dT$ vs T. (d) Heat capacity C_p vs T. Inset: $C_{p/T}$ vs T^2.

We observed two types of temperature-dependent resistivity behaviors from samples we measured from batch A to batch E. One type is with only one resistive anomaly, the other type shows two resistive anomalies. Figures 2(a) and 2(b) show the normalized resistivity curves of each type, $\rho(T)/\rho(400\,\mathrm{K})$ of piece A (PA) from batch A and piece B (PB) from batch B. More temperature-dependent resistance curves of each batch can be found in the Supplemental Materials [31]. Figure 2(a) shows only one resistivity drop in PA, suggesting the existence of one phase transition. The derivative of the resistivity, $d\rho/dT$, shows a sharp kink at 360 K. On the other hand, PB shows two resistive anomalies, suggesting the occurrence of two successive phase transitions. The $d\rho/dT$ plot indicates that one kink appears around 320 K and the other occurs around 230 K. Table I summarizes the number of resistivity anomalies in the ORT phase from each growth trial. From the summary and all temperature-dependent resistivity curves we measured [31], we can see the quality of the single crystal is very sensitive to the nominal concentration of Cu/Mn/As. Only when the starting As concentration is a little less than the stoichiometric concentration in the flux growth (batch A), the resulting single crystals show only one resistive anomaly around 360 K, consistent with the polycrystalline sample [20] and suggesting the high quality of the sample. Even for batch E where only one resistive anomaly exists, the anomaly occurs around 300 K, which is 60 K lower than the one in the polycrystalline sample, suggesting poorer sample quality than the ones in batch A.

The inset of Fig. 2(a) shows the field-dependent Hall resistivity $\rho_{yx}(H)$ of PA at 2 and 100 K. ρ_{yx} is positive, indicating that holes dominate the transport. It is linearly proportional to H and shows almost no temperature dependence, suggesting the validity of the single-band model here. Based on $n = B/e\rho_{yx}$, the estimated carrier density is $\approx 6.5\times10^{20}/\mathrm{cm}^3$. This value is significantly greater than Dirac semimetals Cd_3As_2 [32], Na_3Bi [33], and Weyl semimetal TaAs [34], but comparable to the Dirac nodal-line semimetal candidates ZrSiSe [35] and CaAgAs [36].

TABLE II. Single-crystal crystallographic data of PA and PB in the ORT *Pnma* space group at 300 K.

CuMnAs	PA	PB
F.W. (g/mol)	190.22	190.05
a(Å)	6.5716(4)	6.5868(4)
b(Å)	3.8605(2)	3.8542(3)
c(Å)	7.3047(4)	7.3015(5)
V (Å^3)	185.32(2)	185.36(6)
No. reflections; R_{int}	1624; 0.0210	2189; 0.0304
R_1; wR_2	0.0172; 0.0342	0.0227; 0.0459
Goodness of fit	1.154	1.047

The temperature-dependent susceptibility $[M/H(T)]$ and heat capacity $[C_p(T)]$ of PB are presented in Figs. 2(c) and 2(d). Two slope changes can also be observed in the $M/H(T)$ data, which can be clearly seen in $d(M/H)/dT$. From 300 to 400 K, the highest temperature we measured, the $M/H(T)$ data are almost temperature independent, showing no Curie-Weiss behavior. The $C_p(T)$ data show only one heat-capacity jump around 320 K without any anomaly at 230 K, suggesting that the phase transition at 230 K is most likely a transition between two ordered phases. Since both phase transitions are at high temperatures, we fitted the C_p/T data from 2 to 10 K using $C_p = \gamma T + \alpha T^3 + \beta T^5$, where the first term refers to the electronic heat capacity and the rest to the low-temperature lattice heat capacity. We deduced a Sommerfeld coefficient $\gamma = 1.88\ \mathrm{mJ\,mol^{-1}\,K^{-2}}$ which indicates a small density of states at the Fermi level for the ORT CuMnAs.

To understand why the physical properties are so sensitive to the growth condition, single-crystal x-ray- and neutron-diffraction measurements were performed on PA and PB to investigate their structural properties. No structural phase transition is detected down to 100 K. To determine the stoichiometry of the samples, five different structural models were used in the refinement. Model I assumes vacancies on both Cu and Mn sites. Model II assumes Mn on Cu sites. Model III assumes Cu on Mn sites. Model IV assumes Cu vacancy and Cu on Mn sites. Model V assumes Mn vacancies and Mn on Cu sites. It turns out that Models I, II, and III give the best refinements using single-crystal x-ray-diffraction data. Combined with the SEM-EDX data, which give $Cu_{0.98(3)}Mn_{0.98(4)}As_{1.02(4)}$ for both PA and PB, we are convinced that both site vacancies and site disorders exist. Tables II and III summarize the refined crystal structure, atomic positions, and site occupancies of PA and PB. The major difference between them is the stoichiometry. PA has fully occupied Mn sites with 5.0(2)% of Cu site vacancies, leading to a chemical formula of $Cu_{0.95}MnAs$, while PB has

TABLE III. Atomic coordinates and equivalent isotropic displacement parameters of PA and PB at 300 K. U_{eq} is defined as 1/3 of the trace of the orthogonalized U_{ij} tensor (Å^2).

Atom	Site	SOF	x	y	z	U_{eq}
			PA: $Cu_{0.95}MnAs$			
Cu	4c	0.950(2)	0.37684(6)	1/4	0.05894(5)	0.0120(1)
Mn	4c	1	0.46024(7)	1/4	0.67737(6)	0.0121(2)
As	4c	1	0.25394(4)	1/4	0.37525(4)	0.0080(1)
			PB: $Cu_{0.98}Mn_{0.96}As$			
Cu	4c	0.977(3)	0.3770(1)	1/4	0.0590(1)	0.0120(2)
Mn	4c	0.964(4)	0.4589(1)	1/4	0.6773(1)	0.0122(2)
As	4c	1	0.2544(1)	1/4	0.3754(1)	0.0079(1)

vacancies in both Cu and Mn sites with a chemical formula of $Cu_{0.98}Mn_{0.96}As$. In the rest of the paper, we will denote $Cu_{0.95}MnAs$ as PA and $Cu_{0.98}Mn_{0.96}As$ as PB. The difference in the physical properties between PA and PB most likely arises from the stoichiometry of the Mn and Cu sites. It is worth noting that due to the similar atomic number of Cu and Mn, it is hard to get reliable information on the Cu/Mn site disorder just by single-crystal x-ray-diffraction data. Therefore, the single-crystal neutron-diffraction data were used to investigate the extent of Cu/Mn site mixing here. Considering the number of vacancies revealed by single-crystal x-ray diffraction, the refinement of the neutron-diffraction data suggests 6% of site disorder in PB and 5% of site disorder in PA.

To unravel the nature of these phase transitions, we performed single-crystal neutron-diffraction experiments. Figure 3(a) presents the rocking curve scan at (1,1,0) on PA. The fact that the peak shows up at (1,1,0) at 150 K but not at 400 K indicates that long-range antiferromagnetic order exists at 150 K. The temperature-dependent (1,1,0) peak intensity agrees well with the $d\rho/dT$, shown in Fig. 3(b). It suggests a second-order AFM phase transition and can be fitted using the power law $I(T)/I_0 = [M(T)/M_0]^2 = A + (1 - T/T_N)^{2\beta}$, where M_0 is the saturation moment. With $T_N = 360$ K, the critical exponent is $\beta = 0.35(3)$, which agrees with the ϕ^4 model in three dimensions [37] and suggests the breakdown of the mean-field theory ($\beta = 0.5$) and thus a strong spin fluctuation near T_N. We refined the magnetic and nuclear structure of $Cu_{0.95}MnAs$ together based on 76 effective magnetic reflections. $Pn'ma$ is the only magnetic symmetry which can fit the data. The R factor is 0.0508 and the goodness of fit is 6.08. The refined propagation vector is $\mathbf{k} = 0$, indicating the commensurate antiferromagnetism (CAFM) here [38] and the unit cell of the magnetic structure coincides with the crystal structure. Figures 3(c) and 3(d) show the refined CAFM structure. Mn spins sit on a distorted honeycomb sublattice and order parallel to each other along the b axis [Fig. 3(c)] with the nearest-neighboring spins antiferromagnetically aligned to each other [Fig. 3(d)]. This magnetic structure is the same as the one proposed theoretically in Ref. [16], but with the spin orientation along the b axis. The refined magnetic moment at 150 K is $4.0(1)\mu_B$/Mn.

Figures 4(a) and 4(b) show the rocking curve scan at (1,1,0) on PB. The (1,1,0) peak is not allowed by the crystal structure symmetry in the ORT CuMnAs phase, and the

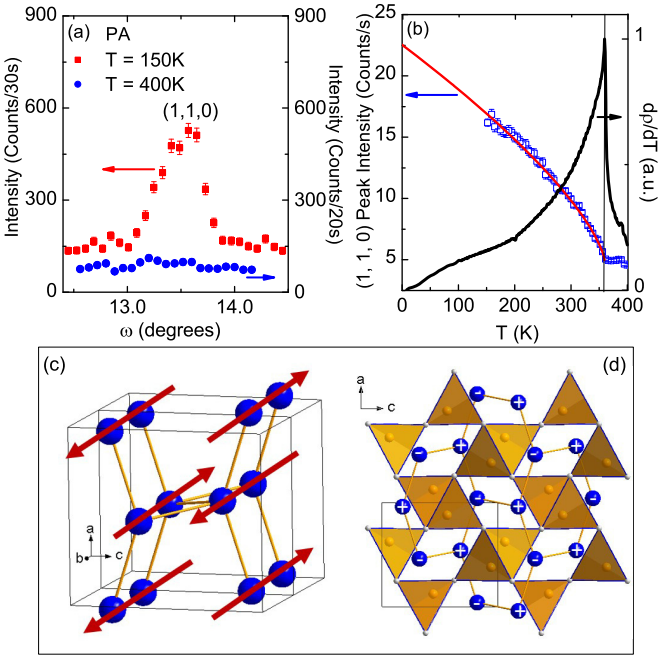

FIG. 3. (a) The (1,1,0) intensity vs ω for PA. (b) A comparison between the (1,1,0) peak intensity and the $d\rho/dT$ vs T. The red line is the power-law fit; see text. (c) Magnetic structure of PA in the CAFM state. Only the Mn sublattice is shown. (d) The view of the magnetic structure from the b direction. Mn atoms are shown in blue. "+" denotes spins pointing out of plane while "−" denotes spin pointing in plane.

nonzero intensity we observed above 320 K is due to the half-wavelength ($\lambda/2$) contamination of the neutron beam [25]. The wavelength of 1.546 Å we used at HB3A is selected by the Si-220 monochromator, which also picks the half-wavelength neutrons that make up 1.4% of the main beam flux at HB3A. In Fig. 4(a), magnetic satellite peaks begin to appear near (1,1,0) as the sample is cooled below 320 K, suggesting incommensurate antiferromagnetism (ICAFM) [38]. Figure 4(c) shows a cut in the $hk0$ plane at 227 K. We can clearly detect the three peaks shown in Fig. 4(a). The concentration of points at (0.9,1,0) and (1.1,1,0) indicates the presence of the incommensurate magnetic peaks, suggesting an incommensurate propagation vector $\mathbf{k} = (0.1,0,0)$. Upon further cooling of the sample below 230 K, we observe that both (0.9,1,0) and (1.1,1,0) peak intensities decrease while the (1,1,0) peak intensity starts to increase, indicating a competition between the CAFM with the propagation vector $\mathbf{k} = 0$ and ICAFM. Below 190 K, both (0.9,1,0) and (1.1,1,0) peaks diminish whereas the (1,1,0) peak keeps increasing, suggesting the disappearance of ICAFM. To better visualize the competition and coexistence, Figure 4(d) shows the (0.9,1,0) and (1,1,0) peak intensities and $d\rho/dT$ as a function of temperature. We can see that $Cu_{0.98}Mn_{0.96}As$ undergoes a second-order paramagnetism (PM) to ICAFM phase transition at 320 K as well as a second-order ICAFM to CAFM phase transition at 230 K. ICAFM competes and coexists with the CAFM phase between 230 and 190 K and disappears below 190 K. Based on 102 effective magnetic peaks, the refined CAFM structure is the same as the one in $Cu_{0.95}MnAs$ [Figs. 3(c) and 3(d)] with the refined magnetic moment at 6 K as $4.3(2)\mu_B$/Mn and a

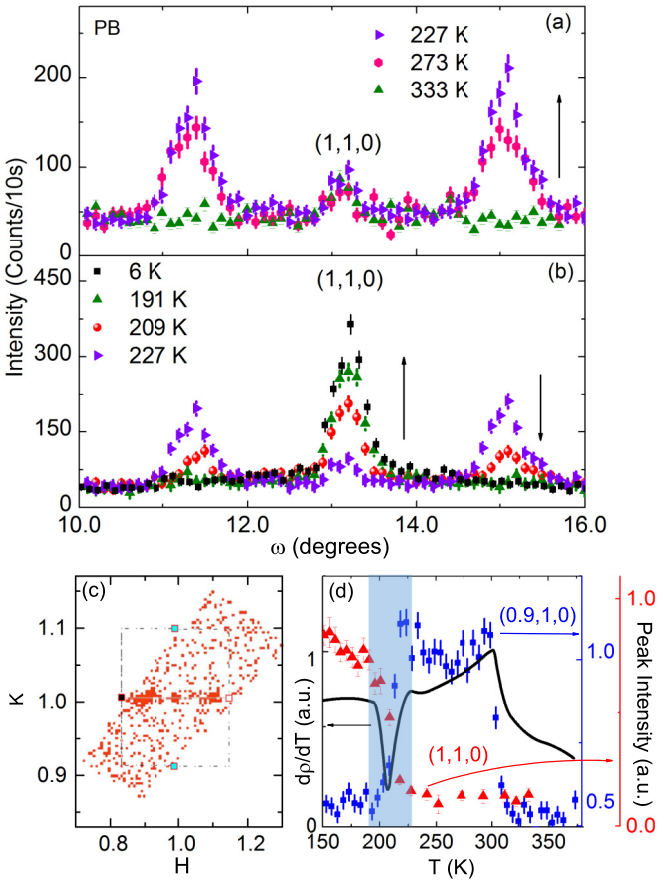

FIG. 4. (a), (b) Intensity vs ω for PB. The black arrows indicate the trend of the peak intensity with decreasing temperature. (c) A cut of the neutron scattering in the $hk0$ plane. (d) A comparison between the (0.9,1,0) peak intensity and $d\rho/dT$ vs T. The light blue box marks the temperature region where CAFM and ICAFM compete and coexist.

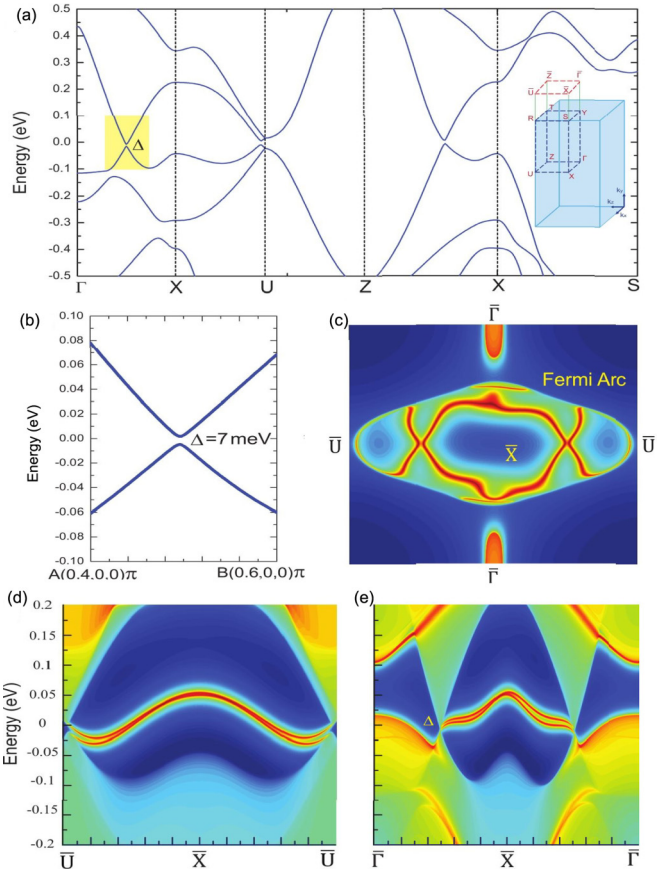

FIG. 5. (a) Calculated band structures of the ORT CuMnAs with SOC and the magnetic structure shown in Fig. 3(c). Inset is the Brillouin zone and its projection to the (010) surface. Δ is the band gap of massive topological fermion along ΓX line. (b) Zoom-in view of the band structure marked by yellow box in (a). (c) Fermi-surface contour on the (010) surface at the calculated Fermi level. Corresponding electronic spectra along (d) $\bar{k}_x = \pi/a$ and (e) $\bar{k}_z = 0$. Fermi level is set to zero.

R factor of 0.0555. The moment is smaller than $5\mu_B$/Mn, the theoretical saturation moment for Mn^{2+}.

IV. DISCUSSION

Based on the magnetic structure and easy axis determined experimentally, in order to explore the electronic and topological properties of ORT CuMnAs with the magnetic orientations along b axis, we recalculate its bulk band structures and the corresponding (010) surface states. Although no chemical disorder or vacancies are considered in the DFT calculation, since the material still holds the translational symmetry and maintains the ORT structures, the electronic structure and surface states shown in Fig. 5 should capture the main character. Due to the presence of the $\mathcal{PT}$ symmetry in the experimental CAFM phase, every bulk state is doubly degenerate. Furthermore, the band inversion still exists in this system, thus the nontrivial topological properties can appear. Because the CAFM order breaks the nonsymmorphic gliding symmetry R_y and screw symmetry S_{2z}, in contrast to the case with spin orientation along the c axis [16], now the gapless coupled Weyl fermions disappear and the Dirac nodal line is fully gapped everywhere by SOC in the bulk Brillouin zone (BZ), as shown in Fig. 5(a). The gap size however is quite small. For example, the band gap induced by SOC along the ΓX line is just 7 meV, as indicated in Fig. 5(b). Figure 5(c) shows the spin-polarized surface states emerging from the gapped bulk states [see Figs. 5(d) and 5(e)] on the (010) side surface. Due to the absence of rotational symmetries on the (010) surface, the Fermi-surface contour at the Fermi level is asymmetric, and the spin-polarized surface states are gapped. This distinguishing character is different from surface states in topological insulators and Dirac semimetals. On the other hand, because the bulk Dirac fermions in this case are massive and the time-reversal symmetry is broken, the fluctuations could resemble the dynamical axion field, which gives rise to exotic modulation of the electromagnetic field showing a similar signature to axion insulators [39].

V. CONCLUSION

In conclusion, the Dirac antiferromagnetic semimetal candidates, ORT $Cu_{0.95}MnAs$ and $Cu_{0.98}Mn_{0.96}As$ single crystals, show no structural phase transitions down to 100 K. The

magnetism is very sensitive to the stoichiometry of the Cu and Mn sites. $Cu_{0.95}MnAs$ has a PM to CAFM phase transition at 360 K while an intermediate ICAFM state between PM and CAFM states appears in $Cu_{0.98}Mn_{0.96}As$. In both CAFM states, spins order parallel to one another along the b axis, but antiparallel to their Mn nearest neighbors with the moment around $4.3\mu_B$/Mn. The spin orientations are along the b axis, which break both S_{2z} and R_y symmetries in the CAFM state and gap the coupled Weyl nodes and Dirac nodal line, resulting in a similar electromagnetic response to that of axion insulators. Furthermore, the presence of spin-polarized surface states on this AFM semimetal makes ORT CuMnAs a good candidate for the antiferromagnetic spintronic applications.

Note added. Recently, we became aware of a subsequent work on orthorombic CuMnAs [40]. Here, orthorombic CuMnAs single crystals with only one phase transition at 310 K were made. Anisotropic susceptibility was studied and led to the conclusion that the easy axis is in the bc plane; heat-capacity and magnetotransport measurements were done and led to the conclusion of massive Dirac fermions. Since the magnetic structure determined in our work has an easy axis along the b axis, this naturally explained their results.

ACKNOWLEDGMENTS

Work at UCLA was supported by the U.S. Department of Energy (DOE), Office of Science, Office of Basic Energy Sciences under Award No. DE-SC0011978. Work at ORNL′s High Flux Isotope Reactor was sponsored by the Scientific User Facilities Division, Office of Basic Energy Sciences, DOE. The research at LSU was supported by the LSU-startup funding and Louisiana Board of Regents Research Competitiveness Subprogram under Contract No. LEQSF (2017-20)-RD-A-08. P.Z. and S.C.Z. acknowledge FAME, one of six centers of STARnet, a Semiconductor Research Corporation program sponsored by MARCO and DARPA. N.N. thanks Dr. Y. Wang for useful discussion.

[1] S. Borisenko, Q. Gibson, D. Evtushinsky, V. Zabolotnyy, B. Buchner, and R. J. Cava, Phys. Rev. Lett. **113**, 027603 (2014).
[2] M. Neupane, S.-Y. Xu, R. Sankar, N. Alidoust, G. Bian, C. Liu, I. Belopolski, T.-R. Chang, H.-T. Jeng, H. Lin *et al.*, Nat. Commun. **5**, 3786 (2014).
[3] Z. K. Liu, B. Zhou, Y. Zhang, Z. J. Wang, H. M. Weng, D. Prabhakaran, S.-K. Mo, Z. X. Shen, Z. Fang, X. Dai *et al.*, Science **343**, 864 (2014).
[4] J. Xiong, S. K. Kushwaha, T. Liang, J. W. Krizan, M. Hirschberger, W. Wang, R. J. Cava, and N. P. Ong, Science **350**, 413 (2015).
[5] K. Wang, D. Graf, H. Lei, S. W. Tozer, and C. Petrovic, Phys. Rev. B **84**, 220401 (2011).
[6] K. Wang, D. Graf, L. Wang, H. Lei, S. W. Tozer, and C. Petrovic, Phys. Rev. B **85**, 041101 (2012).
[7] K. Wang, D. Graf, and C. Petrovic, Phys. Rev. B **87**, 235101 (2013).
[8] S. Borisenko, D. Evtushinsky, Q. Gibson, A. Yaresko, T. Kim, M. N. Ali, B. Büchner, M. Hoesch, and R. J. Cava, arXiv:1507.04847 (2015).
[9] J. Y. Liu, J. Hu, Q. Zhang, D. Graf, H. B. Cao, S. M. A. Radmanesh, D. J. Adams, Y. L. Zhu, G. F. Cheng, X. Liu *et al.*, Nat. Mater. **16**, 905 (2017).
[10] J. Liu, J. Hu, H. Cao, Y. Zhu, A. Chuang, D. Graf, D. J. Adams, S. M. A. Radmanesh, L. Spinu, I. Chiorescu, and Z. Mao, Sci. Rep. **6**, 30525 (2016).
[11] H. Masuda, H. Sakai, M. Tokunaga, Y. Yamasaki, A. Miyake, J. Shiogai, S. Nakamura, S. Awaji, A. Tsukazaki, H. Nakao *et al.*, Sci. Adv. **2**, e1501117 (2016).
[12] S. Huang, J. Kim, W. A. Shelton, E. W. Plummer, and R. Jin, Proc. Natl. Acad. Sci. USA **114**, 6256 (2017).
[13] M. Hirschberger, S. Kushwaha, Z. Wang, Q. Gibson, S. Liang, C. A. Belvin, B. A. Bernevig, R. J. Cava, and N. P. Ong, Nat. Mater. **15**, 1161 (2016).
[14] T. Suzuki, R. Chisnell, A. Devarakonda, Y.-T. Liu, W. Feng, D. Xiao, J. W. Lynn, and J. G. Checkelsky, Nat. Phys. **12**, 1119 (2016).
[15] L. M. Schoop, A. Topp, J. Lippmann, F. Orlandi, L. Muechler, M. G. Vergniory, Y. Sun, A. W. Rost, V. Duppel, M. Krivenkov, S. Sheoran, P. Manuel, A. Varykhalov, B. Yan, R. K. Kremer, C. R. Ast, and B. V. Lotsch, arXiv:1707.03408 (2017).
[16] P. Tang, Q. Zhou, G. Xu, and S.-C. Zhang, Nat. Phys. **12**, 1100 (2016).
[17] L. Šmejkal, J. Železný, J. Sinova, and T. Jungwirth, Phys. Rev. Lett. **118**, 106402 (2017).
[18] P. Wadley, V. Hills, M. R. Shahedkhah, K. W. Edmonds, R. P. Campion, V. Novák, B. Ouladdiaf, D. Khalyavin, S. Langridge, V. Saidl *et al.*, Sci. Rep. **5**, 17079 (2015).
[19] P. Wadley, B. Howells, J. Železný, C. Andrews, V. Hills, R. P. Campion, V. Novák, K. Olejník, F. Maccherozzi, S. S. Dhesi *et al.*, Science **351**, 587 (2016).
[20] F. Máca, J. Mašek, O. Stelmakhovych, X. Martí, H. Reichlová, K. Uhlirová, P. Beran, P. Wadley, V. Novák, and T. Jungwirth, J. Magn. Magn. Mater. **324**, 1606 (2012).
[21] K. Uhlirová, R. Tarasenko, F. Javier Martínez-Casado, B. Vondracková, and Z. Matěj, J. Alloys Compd. **650**, 224 (2015).
[22] P. C. Canfield and Z. Fisk, Philos. Mag. B **65**, 1117 (1992).
[23] SHELXTL, version 6.10, Bruker AXS Inc.: Madison, WI, 2000.
[24] G. M. Sheldrick, Acta Crystallogr. Sect. A **64**, 112 (2008).
[25] B. C. Chakoumakos, H. Cao, F. Ye, A. D. Stoica, M. Popovici, M. Sundaram, W. Zhou, J. S. Hicks, G. W. Lynn, and R. A. Riedel, J. Appl. Crystallogr. **44**, 655 (2011).
[26] J. M. Perez-Mato, S. V. Gallego, E. S. Tasci, L. Elcoro, G. de la Flor, and M. I. Aroyo, Annu. Rev. Mater. Res. **45**, 217 (2015).
[27] J. Rodríguez-Carvajal, Phys. B (Amsterdam, Neth.) **192**, 55 (1993); program available at http://www.ill.fr/dif/Soft/fp/.
[28] P. E. Blöchl, Phys. Rev. B **50**, 17953 (1994).
[29] G. Kresse and J. Furthmüller, Phys. Rev. B **54**, 11169 (1996).
[30] A. A. Mostofi, J. R. Yates, Y.-S. Lee, I. Souza, D. Vanderbilt, and N. Marzari, Comput. Phys. Commun. **178**, 685 (2008).
[31] See Supplemental Material at http://link.aps.org/supplemental/10.1103/PhysRevB.96.224405 for the resistance data of batches PA to PE.

[32] T. Liang, Q. Gibson, M. N. Ali, M. Liu, R. J. Cava, and N. P. Ong, Nat. Mater. **14**, 280 (2014).
[33] J. Xiong, S. Kushwaha, J. Krizan, T. Liang, R. J. Cava, and N. P. Ong, Europhys. Lett. **114**, 27002 (2016).
[34] C. L. Zhang, S.-Y. Xu, I. Belopolski, Z. Yuan, Z. Lin, B. Tong, G. Bian, N. Alidoust, C.-C. Lee, S.-M. Huang *et al.*, Nat. Commun. **7**, 10735 (2016).
[35] J. Hu, Z. Tang, J. Liu, X. Liu, Y. Zhu, D. Graf, K. Myhro, S. Tran, C. N. Lau, J. Wei *et al.*, Phys. Rev. Lett. **117**, 016602 (2016).
[36] E. Emmanouilidou, B. Shen, X. Deng, T.-R. Chang, A. Shi, G. Kotliar, S.-Y. Xu, and N. Ni, Phys. Rev. B **95**, 245113 (2017).
[37] G. A. Baker, B. G. Nickel, and D. I. Meiron, Phys. Rev. B **17**, 1365 (1978).
[38] T. Chatterji, in *Neutron Scattering from Magnetic Materials*, edited by T. Chatterji (Elsevier, Amsterdam, 2006), Chap. 2.
[39] R. Li, J. Wang, X.-L. Qi, and S.-C. Zhang, Nat. Phys. **6**, 284 (2010).
[40] X. Zhang, S. Sun, and H. Lei, Phys. Rev. B **96**, 235105 (2017).